Delocalized metal-oxygen π-redox is the origin of anomalous non-hysteretic capacity in Li-ion and Na-ion cathode materials

Daniil A. Kitchaev,* Julija Vinckeviciute, and Anton Van der Ven*

Materials Department, University of California, Santa Barbara, California 93106, USA

E-mail: dkitch@ucsb.edu; avdv@ucsb.edu

Abstract

The anomalous capacity of Li-excess cathode materials has ignited a vigorous debate over the nature of the underlying redox mechanism, which promises to substantially increase the energy density of rechargeable batteries. Unfortunately, nearly all materials exhibiting this anomalous capacity suffer from irreversible structural changes and voltage hysteresis. Non-hysteretic excess capacity has been demonstrated in $Na_2Mn_3O_7$ and Li_2IrO_3, making these materials key to understanding the electronic, chemical and structural properties that are necessary to achieve reversible excess capacity. Here, we use high-fidelity random-phase-approximation (RPA) electronic structure calculations and group theory to derive the first fully consistent mechanism of non-hysteretic oxidation beyond the transition metal limit, explaining the electrochemical and structural evolution of the $Na_2Mn_3O_7$ and Li_2IrO_3 model materials. We show that the source of anomalous non-hysteretic capacity is a network of π-bonded metal-d and O-p orbitals, whose activity is enabled by a unique resistance to transition metal migration. The π-network forms a collective, delocalized redox center. We show that the voltage, accessible capacity, and structural evolution upon oxidation are collective properties of

the π-network rather than that of any local bonding environment. Our results establish the first rigorous framework linking anomalous capacity to transition metal chemistry and long-range structure, laying the groundwork for engineering materials that exhibit truly reversible capacity exceeding that of transition metal redox.

Introduction

Electrochemical activity exceeding the limits of conventional transition metal oxidation, first observed in Li-excess materials, is one of the most actively researched routes for dramatically increasing the energy density of conventional Li- and Na-ion cathode materials.[1–5] Materials relying in part on this phenomenon avoid the composition and voltage limits of transition metal electrochemistry,[6,7] and achieve some of the highest energy densities reported to date.[4] Several redox mechanisms have been conceived to account for the anomalous capacity of Li-excess materials and related Na intercalation compounds. The anion redox hypothesis attributes the excess capacity to redox on O-p orbitals that are not σ-bonded to a transition metal.[8,9] Numerous proposals exist for how such oxygen-centric oxidation may proceed: formation of localized O-holes, O-O dimerization into peroxo-like structures or true peroxides, or the formation of trapped O_2 molecules or superoxide ions.[1,2,10–13] Competing hypotheses argue that the excess capacity is coupled to structural changes of the electrode, such as metal migration due to the formation of highly-oxidized transition metal ions,[14] or O_2 evolution and densification.[15,16]

Despite their tremendous promise, most electrode chemistries that exhibit an anomalous excess capacity suffer structural changes and irreversibilities due to the loss of O_2 and transition metal migration. Advancements in the suppression of metal migration,[3,15,17] surface protection,[5] and fluorination[18,19] have led to the development of cathodes that maintain an excess capacity over a large number of cycles. Nevertheless, these materials universally exhibit a large voltage hysteresis, signifying the existence of a thermodynamic asymmetry between their charge and discharge mechanisms that remains poorly understood and that

continues to cloud efforts to identify the true origins of the anomalous capacity.

While the vast majority of electrode materials that boast an anomalous capacity are plagued by irreversibilities, there are two notable exceptions: Li_2IrO_3[11,20] and $Na_2Mn_3O_7$.[21,22] Both compounds can access a capacity that exceeds that of conventional transition metal redox without voltage hysteresis, making them unique model systems to identify a redox mechanism that may dramatically increase the energy densities of rechargeable batteries. Although localized and atom-centric theories have been invoked to account for the anomalous capacity in Li_2IrO_3 and $Na_2Mn_3O_7$, they are unable to explain important experimental observations and suffer from internal inconsistencies. For example, the structural evolution of Li_2IrO_3 has been used to argue in favor of O-O dimerization,[11] but these distortions are not present in $Na_2Mn_3O_7$.[23] The formation of isolated O-holes have been proposed as the oxidation mechanism in $Na_2Mn_3O_7$,[21] but this mechanism does not explain the stepped voltage profile of the material, and is inconsistent with the distortions and electronic structure of Li_2IrO_3.[13] More generally, available theories fail to quantitatively explain the strong dependence of the redox process on transition metal chemistry and the long-range structure of the material.[1,2,12,24,25]

Here, we resolve the oxidation mechanism of $Na_2Mn_3O_7$ and Li_2IrO_3. We first show that these two systems are uniquely resistant to transition metal migration as compared to materials known to exhibit hysteresis, suggesting that the oxidation of hysteretic systems is fundamentally tied to structural transformations. We then use high-accuracy GW and random-phase-approximation (RPA) calculations to show that the mechanism of non-hysteretic anomalous redox in $Na_2Mn_3O_7$ is the formation of delocalized π-states that hybridize a network of Mn-*d* and O-*p* orbitals, which we term *π-redox*. Molecular orbital group theory reveals that the π-bonded network forms a large bonding-antibonding gap, creating a high-energy antibonding state that acts as the redox center. The collective behavior of this network is responsible for the multi-step voltage profile observed in $Na_{2-x}Mn_3O_7$ and the structural evolution observed in $Li_{2-x}IrO_3$. Critically, we show that the oxidation potential,

accessible capacity and structural evolution of such a π-bonded network are true collective properties arising from the size and connectivity of the network, rather than the aggregate behavior of local bonding environments. We conclude that in materials where transition metal migration can be suppressed, long-range structure compatible with the formation of large π-networks is the key materials design principle for realizing excess non-hysteretic electrochemistry.

Methods

Electronic structure calculations were performed using the Vienna Ab-Initio Simulation Package (VASP)[26] using the Projected-Augmented Wave (PAW) method.[27] All calculations was converged to 10^{-6} eV in total energy and interatomic forces below 0.02 eV $Å^{-1}$. Structural optimization and broad comparison of π-delocalization to dimerization, metal migration, and O_2 evolution was performed using the SCAN exchange-correlation functional[28] as this method generally yields reliable structures by capturing both local and dispersion forces.[29] Critically, SCAN reliably captures the energetics of both O-O bond formation and the behavior of Mn in highly oxidizing environments.[30] An in-depth discussion of functional choice and the performance of SCAN in reproducing benchmark experimental data as compared to conventional PBE, PBE+U, and HSE methods can be found in Supplementary Discussion 2. All structural optimizations were performed with a reciprocal space discretization of 25 k-points per $Å^{-1}$ without assuming any symmetry. RPA calculations were performed using the adiabatic connection fluctuation-dissipation theorem (ACFDT)[31,32] using 12 frequency points on a 2x2x2 Γ-centered k-point mesh, with respect to the unit cells provided in the Supplementary Information. GW[33] calculations were performed using a single-shot approach (G_0W_0) due to computational limitations, using the same parameters but increasing the number of frequencies to 50. Structure and data processing relied on the pymatgen software package,[34] while the symmetry analysis of distortion modes was performed using

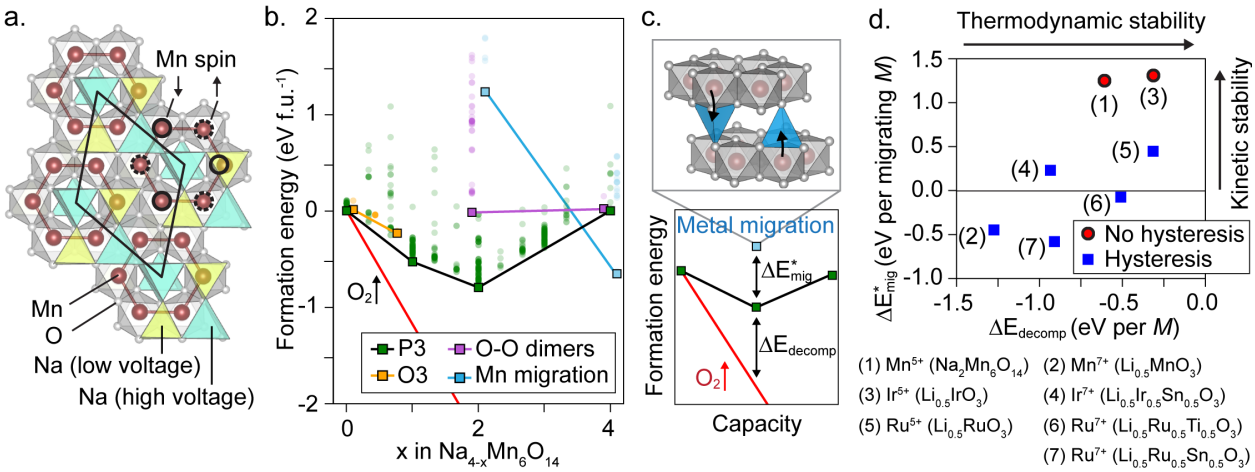

Figure 1: **Structural stability of $Na_{4-x}Mn_6O_{14}$ a.** Structure at $x = 0$, showing Mn-vacancy ordering in the transition metal layer, characteristic magnetic structure, and geometry of Na sites. High-voltage Na sites (cyan) denote Na preserved in the structure throughout the $0 \leq x \leq 2$ region. Red lines denote short Mn-Mn distances within each Mn_6 ring. **b.** Relative energies of structural perturbations, given with respect to P3-$Na_{4-x}Mn_6O_{14}$. Translucent circles denote the energies of all possible configurations, while bold squares highlight the most favorable form of the corresponding perturbation. Points are slightly offset in x for clarity. O_2 evolution is given with respect to O_2 gas at 298K, 1 atm pressure. All energies are obtained from SCAN as described in the Methods and Supplementary Discussion 2. **c.** Schematic of two metrics of structural stability - metal migration energy barrier ΔE^*_{mig} and thermodynamic driving force for O_2 evolution ΔE_{decomp}, with a representative migration mechanism in the common Li_2MO_3 structure. **d.** Computed ΔE_{decomp} and ΔE^*_{mig} for the top of charge in several anion-redox materials, as compared to the experimentally reported voltage hysteresis in their first charge-discharge cycles. The text label indicates the formal oxidation state of the migrating metal ion M and the composition at which ΔE_{decomp} and ΔE^*_{mig} are evaluated.

the ISODISTORT tool.[35]

Results and Discussion

Unique structural stability of $Na_4Mn_6O_{14}$ and Li_2IrO_3 on oxidation

The structure of $Na_{4-x}Mn_6O_{14}$ is defined by a stacking of alternating O-Mn-O and Na layers. The Mn layer consists of a $\sqrt{7}a \times \sqrt{7}a$ Mn-vacancy ordering on a triangular lattice as shown in Figure 1a. The Mn atoms surrounding a vacancy form a cluster of 6 Mn connected by short bonds (2.76 Å), defining a hexagonal superlattice of Mn_6 rings weakly connected

to each other by long Mn-Mn bonds (2.92 Å). Because this Mn_6 ring is the key structural unit in our analysis, we refer to $Na_2Mn_3O_7$ as $Na_4Mn_6O_{14}$. Each Mn_6 ring adopts an antiferromagnetic (AFM) ordering, with weak frustration between the rings relieved within a larger magnetic supercell. The Mn layers adopt a P3-type stacking, with Na occupying two classes of prismatic sites: strongly-bound sites forming a prismatic dumbbell around the vacancy in the Mn-layer and weakly-bound sites face-sharing with a Mn octahedron. Upon desodiation, the weakly-bound Na are extracted first, comprising the region of experimental interest ($0 \leq x \leq 2$). This structural model is consistent with reported experimental data with the caveat that we find the P3 stacking to be preferable to the commonly reported "as-synthesized" O3 structure even at $x = 0$.[21,23,36] There is evidence that oxidation into the $x > 0$ region is accompanied by the formation of the P3 phase,[23] so the discrepancy at $x = 0$ could arise due to small off-stoichiometry in the experimental sample or slight inaccuracies in our predictions of relative stability. We use the P3 structure at $x = 0$ for the remainder of our analysis but verify that the O3 structure leads to the same conclusions.

The Mn-O framework shown in Figure 1a is preserved on desodiation in the region of experimental interest ($0 \leq x \leq 2$) as all decomposition mechanisms are either thermodynamically or kinetically unfavorable. We consider all commonly proposed scenarios for structural evolution coupled to oxidation in this and similar systems: migration of Mn from the metal layer to the Na-layer, formation of peroxide O-O dimers, and O_2 evolution. The relative energies of these scenarios are shown in Figure 1b.

The equilibrium oxidation pathway is the release of O_2 gas accompanied by structural reorganization into MnO_2. This conversion reaction is kinetically limited, with a lower bound on the activation energy given by the energy of local Mn migration. Mn migration typically proceeds through reduction to $Mn^{2+/3+}$ [37] or the formation of tetrahedral $Mn^{5+/6+/7+}$ as recently proposed in Li_2MnO_3.[14] However, the former mechanism requires an auxiliary source of charge balance, while the latter requires relatively small layer slab spacing so as to accommodate the short Mn-O bonds found in highly oxidized Mn environments. Correspondingly,

we find that Mn migration into the Na layer is highly unfavorable at intermediate states of desodiation ($x \leq 2$), suppressing kinetic pathways to Mn-O rearrangement and O_2 release. An alternative oxidation mechanism is the formation of bound oxidized O-O dimers, such as peroxides and superoxides. While the formation of a single peroxide per Mn_6 is formally charge balanced at $x = 2$, enumeration of all possible O-O dimers in the Mn_6 ring does not yield any low energy states. Note that here O-O dimers refer to true peroxides, i.e. O-O bonds below 1.7Å. In summary, taking the energies of the possible decomposition pathways into consideration, structure-preserving desodiation is likely stable in the $0 \leq x \leq 2$ region with respect to all local structural perturbations, rationalizing the exceptional structural stability observed experimentally in this system.[23]

The structural stability of $Na_4Mn_6O_{14}$ at the top of charge, which we define as the resistance to transition metal migration, is similar to that of Li_2IrO_3, and much better than that of other well-studied hysteretic excess-capacity materials. We define two metrics to evaluate the likelihood of structural changes in the oxidized structure, shown schematically in Figure 1c. ΔE_{decomp} defines the energy of decomposition by O_2 evolution and densification and thereby quantifies the average driving force acting on each transition metal M. ΔE^*_{mig} defines the activation energy for transition metal migration from an initial octahedral site to an adjacent tetrahedral site, providing a lower bound on the kinetic barrier to decomposition. We compare these two metrics to the asymmetry in reported first-cycle voltage curves in $Na_4Mn_6O_{14}$,[23] Li_2IrO_3,[11] $Li_2(Ir,Sn)O_3$,[13] Li_2RuO_3,[10,11] $Li_2(Ru,Ti)O_3$,[10] $Li_2(Ru,Sn)O_3$[10] and Li_2MnO_3.[38] The Li-based materials share the Li_2MO_3 honeycomb structure, so they can be used to estimate ΔE_{decomp} and ΔE^*_{mig} from a combination of enumerated and known structures.[11,13,14] The calculated values of ΔE_{decomp} and ΔE^*_{mig}, shown in Figure 1d, suggest that materials that are more susceptible to cation migration than $Na_4Mn_6O_{14}$ and Li_2IrO_3, and that have larger driving forces for O_2 formation, exhibit voltage hysteresis. Moreover, in several cases, cation migration is spontaneous as ΔE^*_{mig} is negative.

The initial metal migration step in the hysteretic materials shown in Figure 1d is driven

by the accessibility of a higher metal oxidation state in tetrahedral sites.[14] It is reasonable to assume that this facile metal migration allows for subsequent rearrangement driving the system towards the equilibrium state of O_2 formation and reduction of the metal, consistent with experimental studies which have correlated voltage hysteresis with structural degradation and O_2 formation.[2,10,13,39] One example is the $Li_2(Ir,Sn)O_3$ system, which develops voltage hysteresis and complex structural rearrangements upon partial substitution of Ir with Sn.[13] We find that $Li_{0.5}Ir_{0.5}Sn_{0.5}O_3$ has a much lower $\Delta E^*_{\mathrm{mig}}$ and higher $\Delta E_{\mathrm{decomp}}$ than $Li_{0.5}IrO_3$ as Sn increases the oxidation state of Ir to 7+ and lowers the barrier for migration through tetrahedral sites. Ru-based systems exhibit a similar trend, but never suppress Ru migration as $\Delta E^*_{\mathrm{mig}}$ remains low in all compositions. This data highlights the key advantage of Na-based materials: while Mn migration in layered Li-cathodes is very favorable as evidenced by Li_2MnO_3, the large layer spacing in $Na_4Mn_6O_{14}$ suppresses this process and allows for structure-preserving, non-hysteretic redox processes to take place.

Oxidation *via* a delocalized π-bonded network of Mn-d and O-p orbitals

Having ruled out structure-altering redox mechanisms in $Na_4Mn_6O_{14}$, we next explore structure-preserving oxidation, whereby the qualitative connectivity of transition metals and oxygens remains unchanged. We find that the mechanism of structure-preserving oxidation is the formation of an electrochemically active π-state, delocalized within the Mn_6 ring and with nearly equal contributions from Mn-d and O-p orbitals. To identify this state, we use a complimentary pair of techniques, GW and RPA. These methods provide highly reliable models of band structure and total energy by directly accounting for electronic correlation,[31–33] which is particularly important in systems exhibiting complex orbital hybridization.[40,41] While both methods are non-empirical, they rely on an initial set of orbitals obtained from a conventional density functional theory (DFT) functional. We use this fact to vary the electronic structure and compare scenarios with differing contributions of Mn and O to the

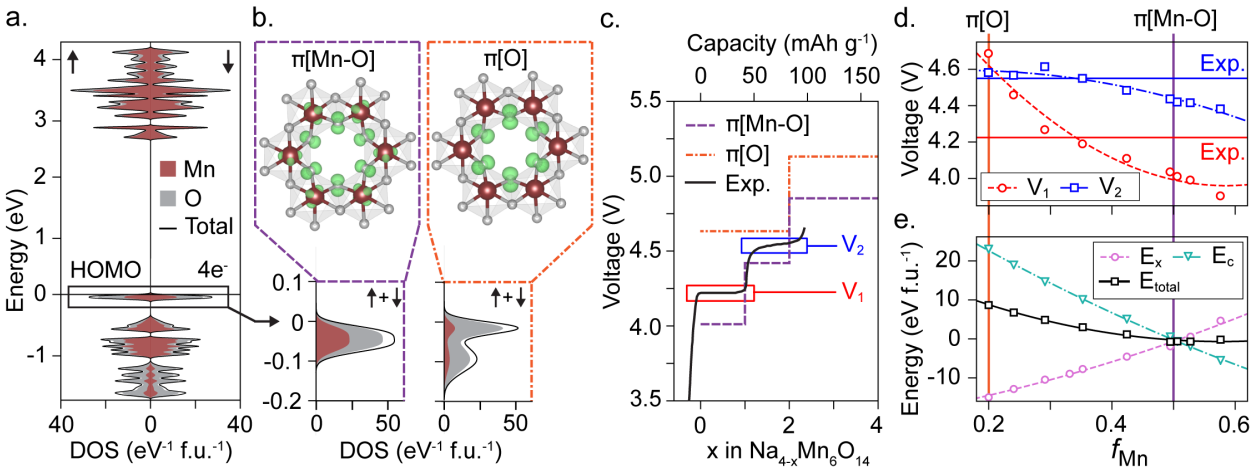

Figure 2: **π[Mn-O] hybridization underlying the electrochemical activity of $Na_4Mn_6O_{14}$. a.** G_0W_0 electronic density of states (DOS) of $Na_4Mn_6O_{14}$, which contains an energetically–isolated highest occupied molecular orbital (HOMO) at the Fermi level. **b.** The degree of Mn-d/O-p hybridization in the HOMO can vary from pure O-p (π[O]) to equal Mn-d/O-p (π[Mn-O]) scenarios. **c.** Voltage profiles computed using RPA corresponding to oxygen-dominated (π[O]) and hybrid Mn-O redox (π[Mn-O]), compared to the experimental first-charge voltage[23] defined by voltage steps V_1 and V_2. The experimental voltage profile is offset slightly in x to align the start of the V_1 plateau with $x = 0$. **d.** Computed voltage steps V_1 and V_2 for intermediate levels of Mn/O hybridization as compared to experimental values. The order parameter f_{Mn} quantifies the degree of Mn contribution to the HOMO and is formally defined in Supplementary Data 2. Trendlines are shown to guide the eye. **e.** Total energy E_{total} for various levels of Mn/O hybridization, decomposed into exchange and correlation energy components, E_x and E_c. Energies are given with respect to the π[Mn-O] scenario. Quadratic fits to E_x, E_c, and E_{total} are shown to guide the eye. Mn/O hybridization is formally defined in Supplementary Data 3.

redox-active state. For example, standard semi-local DFT yields orbitals for the hybridized scenario, while adding a fraction of exact-exchange generates orbitals consistent with O-dominated redox. A full description of this procedure and the functionals used is available in Supplementary Data 2. We then obtain the band structure, total energy, and voltage profile of each scenario from GW and RPA.

We first show that the redox center must be a collective orbital of the Mn_6 ring. The electronic structure of the sodiated $Na_4Mn_6O_{14}$ endpoint is shown in Figure 2a as a plot of the density of states (DOS). A critical feature of this spectrum, independent of the choice of initial orbitals, is a narrow-energy state at the Fermi level, the highest occupied molecular

orbital (HOMO). This state accounts for 4 electrons per Mn_6 and has the full symmetry of the 6-fold ring. The combination of 6-fold symmetry and 4-fold occupancy cannot be obtained from any combination of localized states, meaning that the HOMO must be a delocalized orbital.

We next use the voltage profile and total energy minimization to show that this state is defined by π-bonding with equal contributions from Mn-d and O-p orbitals. The two limiting cases, majority O-p character (π[O]) and equal Mn-d/O-p character (π[Mn-O]), are shown in Figure 2b, plotted as the charge density associated with the HOMO and projections of the total DOS onto Mn-d and O-p orbitals. These two scenarios yield qualitatively different electrochemical voltage profiles, as shown in Figure 2c. The experimental first-charge voltage is defined by two plateaus, marked V_1 and V_2. The hybridized π[Mn-O] scenario similarly predicts two plateaus, while the O-dominated π[O] case gives a single high-voltage plateau inconsistent with experiment. The best agreement with experimental voltage is given by an intermediate scenario with at least 33% Mn contribution to the HOMO, as shown in Figure 2d. The origin of the two voltage plateaus is a magnetic stabilization of the $x = 1$ state, as discussed in detail in Supplementary Data 3. Independent of the voltage, the hybridized π[Mn-O] scenario is favorable from a total energy standpoint. As shown in Figure 2e, exchange energy (E_x) favors the pure oxygen picture, while correlation energy (E_c) drives hybridization with Mn-d states. The total energy is minimized at approximately equal Mn/O contributions, corresponding to the hybridized π[Mn-O] state. This mechanism suggests that oxidation beyond the transition metal limit involves a continuous rehybridization of metal and oxygen states, reminiscent of the behavior of conventional metal oxides.[42–44]

The atomic orbitals which hybridize to form the π[Mn-O] state are shown in Figure 3a. The π-system has D_{3d} symmetry and comprises two subsystems, ρ(Mn) and η(O), consisting of Mn-d and O-p orbitals, respectively. Each Mn atom contributes a single d-orbital, which is one of the non-bonding $t_{2g}^{nb}(O_h)$ levels of the octahedral MnO_6 environment. Each O atom contributes a p orbital which is not σ-bonded to any transition metal.

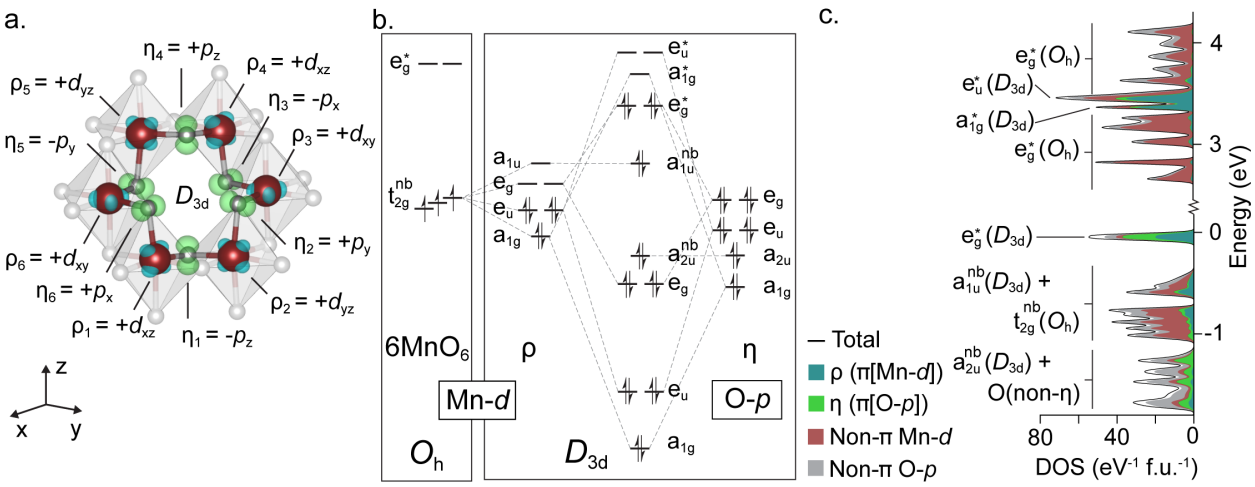

Figure 3: **Symmetry analysis of the π[Mn-O] redox center. a.** Atomic orbitals which hybridize under D_{3d} symmetry to form the redox–active π[Mn-O] state, grouped into ρ and η subsystems for Mn-d and O-p orbitals, respectively. **b.** Molecular orbital diagram for the π[Mn-O] states, arising from the hybridization of the ρ and η subsystems. $*$ denotes antibonding orbitals while nb denotes non-bonding states. **c.** Projection of the $Na_4Mn_6O_{14}$ G_0W_0 DOS onto the ρ and η subsystems, with labels to the corresponding states in the molecular orbital diagram.

The redox-active HOMO is an antibonding orbital corresponding to the 2-fold degenerate e_g irreducible representation of the D_{3d} point group. To derive the energy levels of the combined π system, we first determine the symmetrized orbitals of the ρ(Mn) and η(O) subsystems and then form bonding and antibonding orbitals between states with matching irreducible representations, as described in Supplementary Methods 1 and shown in Figure 3b. By projecting the $Na_4Mn_6O_{14}$ DOS onto the ρ and η subsystems as shown in Figure 3c, we can isolate the predicted π-states from the $t_{2g}^{nb}(O_h)$ and $e_g^*(O_h)$ states arising from octahedral MnO_6 environments. For the energetically-isolated antibonding $e_g^*(D_{3d})$, $a_{1g}^*(D_{3d})$ and $e_u^*(D_{3d})$ orbitals, the integral of the DOS matches the predicted degeneracy of these states. Independently, we confirm that these peaks in the DOS correspond to antibonding Mn-O interactions using crystal-orbital Hamiltonian population (COHP) analysis.[45]

The molecular orbital diagram shown in Figure 3b reveals that the origin of excess capacity in $Na_4Mn_6O_{14}$ is a large bonding-antibonding gap within the delocalized π[Mn-O] system. This gap creates a high-energy antibonding state occupied by 4 electrons per Mn_6

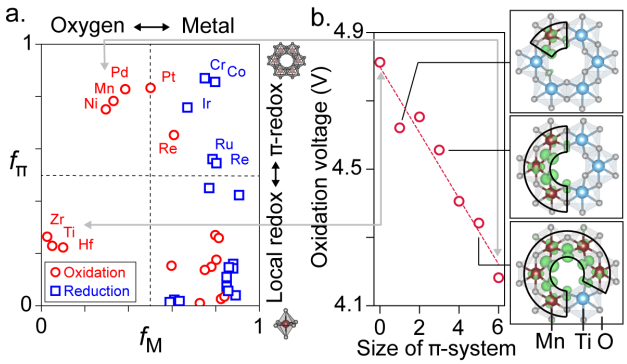

Figure 4: **Behavior of π-redox in transition metal oxides. a.** Redox mechanisms in M_6^{4+} ring environments where M is any $3d$, $4d$, or $5d$ transition metal with a known M^{4+} oxidation state. Unlabeled points include all such metals M not explicitly marked in the other quadrants. Oxidation and reduction mechanisms are evaluated using the relative weight of the π-system in the projected DOS of, respectively, the HOMO and LUMO of hypothetical $Na_4M_6^{4+}O_{14}$ materials. The order parameters f_M and f_π quantify the degree of metal and total π-system contribution and are formally defined in Supplementary Data 2. **b.** Oxidation voltage of removing a single electron from $Na_4Mn_{6-n}Ti_nO_{14}$, where n determines the extent of the π[Mn-O] redox center, shown for $n = 1, 3, 5$. Voltage is computed using RPA based on the calibration given in Figure 2d. A linear fit is shown to guide the eye.

ring, which are accessible electrochemically. The practical capacity of the material is further limited to 2 electrons per Mn_6 ring by the fact that there are only 2 weakly-bound, face-sharing Na in the structure as shown in Figure 1a.

Electrochemical properties of π-redox dictated by network structure

We next show that the π-redox oxidation potential is a true collective property of the π-bonded network, rather than that of any specific bonding environment. To do so, we derive chemical rules dictating the formation of the π-network in a broad range of chemistries and study the effect of interrupting the network with inactive elements.

The π-system is electrochemically relevant when the transition metal $t_{2g}^{\mathrm{nb}}(O_h)$ orbitals are partially occupied, and is most prominent with d^3 and d^6 ions. To separate the impact of chemistry from bonding geometry, we repeat the DOS analysis for isostructural $Na_4M_6^{4+}O_{14}$ materials, where M is any $3d$, $4d$, or $5d$ transition metal with a known M^{4+} oxidation

state. While these materials are hypothetical, their electronic structure is representative of the M_6-ring environments ubiquitous in layered materials. The behavior of these systems is summarized in Figure 4a in terms of f_M and f_π, two order parameters quantifying the contribution of the transition metal and the π-system to the redox-active state (see Supplementary Data 2 for a formal definition). The π-system is active on oxidation when the transition metal has either a d^3 (Mn^{4+}, Re^{4+}) or d^6 (Ni^{4+}, Pd^{4+}, Pt^{4+}) configuration, and similarly on reduction with d^2 (Cr^{4+}) or d^5 (Co^{4+}, Ir^{4+}). Oxidation of d^3 and d^6 metals proceeds via hybridized π-redox, while the oxidation of d^0 systems (Ti^{4+}, Zr^{4+}, Hf^{4+}) does not involve the π-system as the O-p orbitals in the M_6 ring are not energetically distinct from other oxygen states. This behavior is consistent with the hybridization diagram shown in Figure 3b: when the metal $t_{2g}^{nb}(O_h)$ states are filled, the HOMO is a hybridized antibonding orbital, while for d^0 metals, the HOMO is a pure oxygen state as shown in Supplementary Data 4.

A unique feature of π-redox is that the oxidation potential is not determined by any local bonding environment but rather by the total size the delocalized π-system, making voltage a collective property of the network. We probe the impact of π-delocalization by substituting Ti^{4+}, a π-inactive ion, into the Mn_6 ring of $Na_4Mn_6O_{14}$. As shown in Figure 4b, a Mn_nTi_{6-n} ring creates a π-system consisting of n Mn-d and O-p orbitals. The voltage required to remove 1 electron from this system is shown in Figure 4b, by analogy to the first voltage plateau of $Na_{4-x}Mn_6O_{14}$. Formation of a larger π-system lowers the oxidation voltage by increasing the bonding/antibonding gap within the π-orbitals and thus moving the antibonding HOMO to a higher energy. Extrapolating the trend in Figure 4b, it may even be the case that a larger π[Mn-O] system can be oxidized below the typical voltage of O_2 evolution, 3.4-3.8V, making the process thermodynamically favorable relative to O_2 loss.

The dramatic impact of π-network size on oxidation voltage proves that the electrochemical potential of π-redox is primarily a network effect, dictated by the number of building blocks in the network and not the properties of any local environment. This network prop-

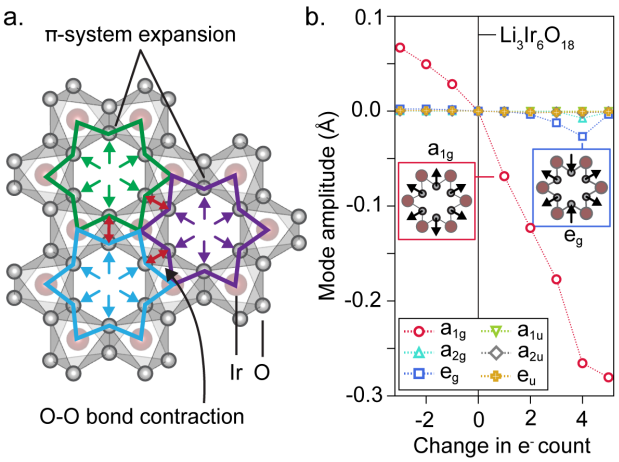

Figure 5: **O-O distance contraction in $Li_{0.5}IrO_3$ caused by π-redox. a.** Distortion of the oxygens in a Ir_6 ring environment on oxidation and reduction, relative to O1-$Li_3Ir_6O_{18}$.[11] **b.** Distortion is quantified by the total amplitude of modes corresponding to each irreducible representation of the D_{3d} point group of the ideal ring environment.

erty cannot be explained by any local bonding theory, such as the recent proposal that local π-bonding between O-p and metal-d orbitals stabilizes localized O-holes.[46]

π-redox reconciles the behavior of Li_2IrO_3 and $Na_2Mn_3O_7$

Delocalized π-redox provides an alternative explanation for the structural distortions that have been observed during oxidation in Li_2IrO_3, which have previously been interpreted as evidence of "peroxo-like" O-O dimers.[11] As shown in Figure 5a, the contraction in O-O distance, seen as a signature of the "peroxo-like" interaction, in fact arises from the homogeneous expansion of the π-redox centers in each Ir_6 ring. To distinguish π-redox from peroxo-like interactions, we evaluate the structural evolution of the oxygens in the Ir_6 ring as electrons are removed from or added to O1-$Li_3Ir_6O_{18}$, which is the oxidized structure of Li_2IrO_3. While both mechanisms lead to structural distortions, π-redox preserves the symmetry of the ring, while oxidation of individual O-O dimers does not. We probe the symmetry of the redox center independently of any changes induced by Li-vacancy ordering by compensating the redox by a uniform background countercharge rather than changing Li content. Figure 5b shows the displacement from O1-$Li_3Ir_6O_{18}$ in terms of the normal modes

that break the various symmetries of the system. Across a wide range of oxidation and reduction, the only active distortion modes are the a_{1g} modes that preserve the symmetry of the ring. This highly symmetric evolution is consistent with the behavior of a delocalized π-redox center, meaning that the experimentally observed reduction in O-O distance is not due to an interaction between those oxygens, but rather due to an expansion of π-hybridized Ir-O rings. The shortening of O-O bonds is a side effect of the geometry of the Ir ordering as shown in Figure 5a. Minor symmetry breaking observed at particular electron counts in Li_2IrO_3 and $Na_4Mn_6O_{14}$ are consistent with Jahn-Teller distortions of the collective π-state, as described in Supplementary Data 3. Finally, it is worth noting that in Li_2IrO_3, oxygens distort away from the ring center while in $Na_4Mn_6O_{14}$ the ring contracts,[23] reflecting the differing connectivity of the π-network between Li_2IrO_3 and $Na_4Mn_6O_{14}$.

More broadly, our results unify a wide range of observations associated with anomalous electrochemical capacity. It is well established that the voltage hysteresis plaguing most Li-excess materials and related Na compounds arises from structural changes due to metal-oxygen bond breaking,[2,13,15,25,47] which has been correlated with transition metal chemistry[48] and the fractional concentration of holes per oxygen.[12] We confirm that the likelihood of metal-oxygen bond breaking is critical to predicting voltage hysteresis and propose two thermochemical predictors of structural stability: the energy of decomposition and the barrier to transition metal migration (Figure 1c). These two thermochemical predictors reveal the existence of strong correlations between transition metal chemistry and the susceptibility of the electrode to structural degradation and voltage hysteresis (Figure 1d). Furthermore, they show that in some cases, transition metal migration may even by triggered by the formation of highly-oxidized metal states such as Mn^{7+}, Ir^{7+} and Ru^{7+}, revealing an alternative redox mechanism that has important and undesirable structural consequences. In cases where the structure is preserved, it has been argued that localized oxygen holes relax by forming peroxo-like O-O bonds or by partial charge transfer to adjacent transition metals.[11,46,48] We have shown that O-O distance shortening observed in Li_2IrO_3[11] is a consequence of π-redox

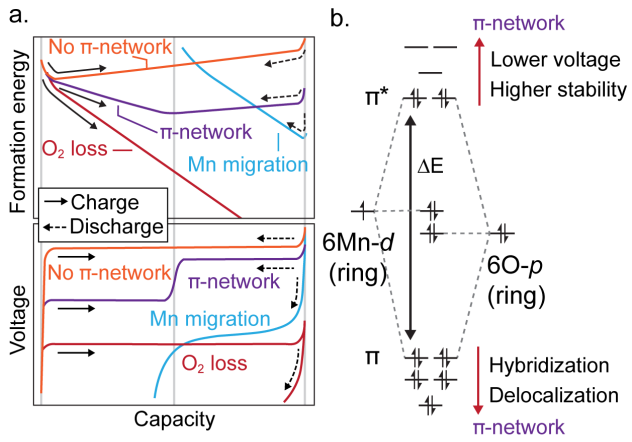

Figure 6: **Non-hysteretic excess capacity from π-redox**. **a.** Schematic of the voltage profiles and corresponding free energies of possible redox mechanisms which may occur on charge and discharge in $Na_{4-x}Mn_6O_{14}$ or a similar material. **b.** Schematic energy-level diagram illustrating how the formation of a π-network leads to lower voltage and improved reversibility.

rather than independent O-O interactions. This behavior contrasts with that of sulfides,[49,50] where we find that structure-preserving anion redox through S-S dimerization is favored over π[S]-redox, as described in Supplementary Discussion 1. Finally, the apparent charge redistribution between transition metals and oxygen reported in a number of systems[46,48] is an artefact of the projection of the delocalized π-state onto atomic orbitals. We have shown that the key properties of the π-redox center arise from its delocalized, network structure and cannot be explained by a locally projected bonding model.

Materials design rules for accessing non-hysteretic excess capacity using π-redox

The absence of voltage hysteresis in $Na_4Mn_6O_{14}$ and Li_2IrO_3 is explained by the stability of the charged material to local structural perturbations. First, formation of the delocalized π-redox center stabilizes the charged state and reduces the driving force for decomposition. Second, the large layer spacing and P3 stacking in $Na_4Mn_6O_{14}$ suppresses Mn migration into the Na layer. While strategies for controlling metal migration have been discussed

elsewhere,[3,14,15,17] the π-redox mechanism leads to several new design rules for engineering materials capable of reversibly providing excess capacity.

The delocalization of Mn and O orbitals into increasingly large π-networks necessarily improves the reversibility of excess oxidation by lowering the oxidation potential and reducing the driving force for decomposition, as summarized schematically in Figure 6a. The presence of a large π-network lowers the average oxidation voltage and creates an initial low-voltage plateau, as compared to materials where such hybridization and delocalization is not possible ("no π-network"). Both effects lower the free energy of the charged state thereby decreasing the driving force for decomposition, as shown in the top panel of Figure 6a. The stabilized charged state in the π-network scenario can then be reduced with minimal voltage hysteresis. In contrast, in materials where the choice of transition metal or crystal structure does not allow metal/O hybridization and π-delocalization ("no π-network" scenario), the unstable charge state is likely to decompose through metal migration or O_2 loss, resulting in a large voltage drop on discharge.

The design of materials with similarly reversible π-redox centers must emphasize the extended connectivity of unbound O-p lobes with transition metal d-orbitals into maximally delocalized π-bonded systems with an antibonding HOMO. The low oxidation voltage of the π-network has its origin in a redox-active orbital that corresponds to a high energy antibonding state, split off from the inaccessible t_{2g}^{nb} and O-p states by a large bonding/antibonding gap in the π-system, as shown schematically in Figure 6b. While "Vacancy-O-Vacancy" environments with unbound O-p lobes[8,9] are a prerequisite to this behavior, delocalization over multiple metal-d and O-p orbitals is essential to lower the voltage and stabilize the oxidized state as illustrated in Figure 6b.

We find that excess oxidation *via* π-redox is most favorable when the transition metal M has either a d^3 or d^6 configuration in its highest conventionally accessible oxidation state, although d^4 and d^5 ions also have some affinity for π-hybridization. Moreover, this process requires that M not be in a d^0 configuration. Mn^{4+} is the most readily accessible transition

metal satisfying these rules. While Ni^{4+} appears to be as good a candidate for oxidation by π-redox as Mn^{4+}, it is very difficult to form ring configurations of Ni^{4+}, as evidenced by the extreme conditions required for the syntheses of Li_2NiO_3.[51] This result indicates that the search for non-hysteretic excess-capacity analogous to $Na_4Mn_6O_{14}$ and Li_2IrO_3 must focus on Mn^{4+} and select other transition metals that are compatible with π-delocalization. While d^0 metals and other π-inactive elements may play other beneficial roles in the material, they are detrimental to oxidation *via* π-redox. Finally, an important open question is how the formation of delocalized π-states proceeds in the presence of dissimilar metals of varying affinity for π-hybridization. For example, while a ring of Co^{4+} does not oxidize via π-redox, the situation may be more favorable in a ring mixing Co^{4+} with Mn^{4+} and Ni^{4+} as expected in some Li-rich Ni-Mn-Co (NMC) cathodes.

Conclusion

We have shown that the origin of anomalous non-hysteretic capacity in $Na_2Mn_3O_7$ and Li_2IrO_3 is a delocalized π-system hybridizing a network of metal-d and O-p orbitals that stabilizes the oxidized state. This effect is synergistic with the suppression of transition metal migration, by the large layer spacing and P3 stacking in the case of $Na_2Mn_3O_7$, and low oxidation state of Ir in the case of Li_2IrO_3. π-redox is the first mechanism to reconcile the behavior of these two model systems for non-hysteretic capacity exceeding the limits of transition metal redox: the unique voltage profile observed in $Na_2Mn_3O_7$, and the characteristic structural evolution reported in Li_2IrO_3. Critically, we have shown that the oxidation potential, accessible capacity, and structural evolution of π-redox is a true collective property of the π-bonded network rather than that of any individual bonding environment. Finally, we argue that the two key materials design principles for realizing non-hysteretic excess capacity in Li- and Na-ion cathode materials is engineering extended networks of unbound O-p lobes and d-orbitals of non-d^0 transition metals, and the suppression of transition metal

migration.

Author contributions

D.A.K., J.V. and A.V.d.V planned the project. D.A.K. performed calculations and analyzed results in consultation with J.V. and A.V.d.V. The manuscript was written by D.A.K. and revised by J.V. and A.V.d.V.

Competing interests

The authors declare no competing interests.

Acknowledgements

J.V. and A.V.d.V acknowledge helpful discussions with Dr. Maxwell Radin. The research reported here was supported by the Materials Research Science and Engineering Center at UCSB (MRSEC NSF DMR 1720256). Computational resources for this project were provided by the National Energy Research Scientific Computing Center, a DOE Office of Science User Facility supported by the Office of Science of the U.S. Department of Energy under Contract No. DE-AC02-05CH11231, as well as the Center for Scientific Computing at UC Santa Barbara, which is supported by the National Science Foundation (NSF) Materials Research Science and Engineering Centers program through NSF DMR 1720256 and NSF CNS 1725797.

References

(1) Assat, G.; Tarascon, J.-M. Fundamental understanding and practical challenges of anionic redox activity in Li-ion batteries. *Nature Energy* **2018**, *3*, 373–386.

(2) House, R. A.; Maitra, U.; Pérez-Osorio, M. A.; Lozano, J. G.; Jin, L.; Somerville, J. W.; Duda, L. C.; Nag, A.; Walters, A.; Zhou, K.-J., et al. Superstructure control of first-cycle voltage hysteresis in oxygen-redox cathodes. *Nature* **2020**, *577*, 502–508.

(3) Eum, D.; Kim, B.; Kim, S. J.; Park, H.; Wu, J.; Cho, S.-P.; Yoon, G.; Lee, M. H.; Jung, S.-K.; Yang, W., et al. Voltage decay and redox asymmetry mitigation by reversible cation migration in lithium-rich layered oxide electrodes. *Nature Materials* **2020**, *19*, 419–427.

(4) Ji, H.; Wu, J.; Cai, Z.; Liu, J.; Kwon, D.-H.; Kim, H.; Urban, A.; Papp, J. K.; Foley, E.; Tian, Y., et al. Ultrahigh power and energy density in partially ordered lithium-ion cathode materials. *Nature Energy* **2020**, *5*, 213–221.

(5) Zhu, Z.; Yu, D.; Yang, Y.; Su, C.; Huang, Y.; Dong, Y.; Waluyo, I.; Wang, B.; Hunt, A.; Yao, X., et al. Gradient Li-rich oxide cathode particles immunized against oxygen release by a molten salt treatment. *Nature Energy* **2019**, *4*, 1049–1058.

(6) Kitchaev, D. A.; Lun, Z.; Richards, W. D.; Ji, H.; Clément, R. J.; Balasubramanian, M.; Kwon, D.-H.; Dai, K.; Papp, J. K.; Lei, T.; McCloskey, B. D.; Yang, W.; Lee, J.; Ceder, G. Design principles for high transition metal capacity in disordered rocksalt Li-ion cathodes. *Energy Environ. Sci.* **2018**, *11*, 2159–2171.

(7) Lun, Z.; Ouyang, B.; Cai, Z.; Clément, R. J.; Kwon, D.-H.; Huang, J.; Papp, J. K.; Balasubramanian, M.; Tian, Y.; McCloskey, B. D.; Ji, H.; Kim, H.; Kitchaev, D. A.; Ceder, G. Design Principles for High-Capacity Mn-Based Cation-Disordered Rocksalt Cathodes. *Chem* **2020**, *6*, 153 – 168.

(8) Luo, K.; Roberts, M. R.; Hao, R.; Guerrini, N.; Pickup, D. M.; Liu, Y.-S.; Edström, K.; Guo, J.; Chadwick, A. V.; Duda, L. C., et al. Charge-compensation in 3d-transition-metal-oxide intercalation cathodes through the generation of localized electron holes on oxygen. *Nature chemistry* **2016**, *8*, 684.

(9) Seo, D.-H.; Lee, J.; Urban, A.; Malik, R.; Kang, S.; Ceder, G. The structural and chemical origin of the oxygen redox activity in layered and cation-disordered Li-excess cathode materials. *Nature chemistry* **2016**, *8*, 692.

(10) Sathiya, M.; Rousse, G.; Ramesha, K.; Laisa, C.; Vezin, H.; Sougrati, M. T.; Doublet, M.-L.; Foix, D.; Gonbeau, D.; Walker, W.; Prakash, A. S.; Ben Hassine, M.; Dupont, L.; Tarascon, J.-M. Reversible anionic redox chemistry in high-capacity layered-oxide electrodes. *Nature materials* **2013**, *12*, 827–835.

(11) McCalla, E.; Abakumov, A. M.; Saubanère, M.; Foix, D.; Berg, E. J.; Rousse, G.; Doublet, M.-L.; Gonbeau, D.; Novák, P.; Van Tendeloo, G.; Dominko, R.; Tarascon, J.-M. Visualization of O-O peroxo-like dimers in high-capacity layered oxides for Li-ion batteries. *Science* **2015**, *350*, 1516–1521.

(12) Yahia, M. B.; Vergnet, J.; Saubanère, M.; Doublet, M.-L. Unified picture of anionic redox in Li/Na-ion batteries. *Nature materials* **2019**, *18*, 496–502.

(13) Hong, J.; Gent, W. E.; Xiao, P.; Lim, K.; Seo, D.-H.; Wu, J.; Csernica, P. M.; Takacs, C. J.; Nordlund, D.; Sun, C.-J., et al. Metal-oxygen decoordination stabilizes anion redox in Li-rich oxides. *Nature materials* **2019**, *18*, 256–265.

(14) Radin, M. D.; Vinckeviciute, J.; Seshadri, R.; Van der Ven, A. Manganese oxidation as the origin of the anomalous capacity of Mn-containing Li-excess cathode materials. *Nature Energy* **2019**, *4*, 639–646.

(15) Sathiya, M.; Abakumov, A. M.; Foix, D.; Rousse, G.; Ramesha, K.; Saubanère, M.; Doublet, M.; Vezin, H.; Laisa, C.; Prakash, A.; Gonbeau, D.; VanTendeloo, G.; Tarascon, J.-M. Origin of voltage decay in high-capacity layered oxide electrodes. *Nature materials* **2015**, *14*, 230–238.

(16) Singer, A.; Zhang, M.; Hy, S.; Cela, D.; Fang, C.; Wynn, T.; Qiu, B.; Xia, Y.; Liu, Z.;

Ulvestad, A., et al. Nucleation of dislocations and their dynamics in layered oxide cathode materials during battery charging. *Nature Energy* **2018**, *3*, 641–647.

(17) Vinckeviciute, J.; Radin, M. D.; Faenza, N. V.; Amatucci, G. G.; Van der Ven, A. Fundamental insights about interlayer cation migration in Li-ion electrodes at high states of charge. *J. Mater. Chem. A* **2019**, *7*, 11996–12007.

(18) House, R. A.; Jin, L.; Maitra, U.; Tsuruta, K.; Somerville, J. W.; Förstermann, D. P.; Massel, F.; Duda, L.; Roberts, M. R.; Bruce, P. G. Lithium manganese oxyfluoride as a new cathode material exhibiting oxygen redox. *Energy Environ. Sci.* **2018**, *11*, 926–932.

(19) Lun, Z.; Ouyang, B.; Kitchaev, D. A.; Clément, R. J.; Papp, J. K.; Balasubramanian, M.; Tian, Y.; Lei, T.; Shi, T.; McCloskey, B. D.; Lee, J.; Ceder, G. Improved Cycling Performance of Li-Excess Cation-Disordered Cathode Materials upon Fluorine Substitution. *Advanced Energy Materials* **2019**, *9*, 1802959.

(20) Pearce, P. E.; Perez, A. J.; Rousse, G.; Saubanère, M.; Batuk, D.; Foix, D.; McCalla, E.; Abakumov, A. M.; Van Tendeloo, G.; Doublet, M.-L.; Tarascon, J.-M. Evidence for anionic redox activity in a tridimensional-ordered Li-rich positive electrode beta-Li 2 IrO 3. *Nature materials* **2017**, *16*, 580–586.

(21) Mortemard de Boisse, B.; Nishimura, S.-i.; Watanabe, E.; Lander, L.; Tsuchimoto, A.; Kikkawa, J.; Kobayashi, E.; Asakura, D.; Okubo, M.; Yamada, A. Highly Reversible Oxygen-Redox Chemistry at 4.1 V in Na4/7-x[Va1/7Mn6/7]O2 (Va: Mn Vacancy). *Advanced Energy Materials* **2018**, *8*, 1800409.

(22) Li, Y.; Wang, X.; Gao, Y.; Zhang, Q.; Tan, G.; Kong, Q.; Bak, S.; Lu, G.; Yang, X.-Q.; Gu, L.; Lu, J.; Amine, K.; Wang, Z.; Chen, L. Native Vacancy Enhanced Oxygen Redox Reversibility and Structural Robustness. *Advanced Energy Materials* **2019**, *9*, 1803087.

(23) Song, B.; Tang, M.; Hu, E.; Borkiewicz, O. J.; Wiaderek, K. M.; Zhang, Y.; Phillip, N. D.; Liu, X.; Shadike, Z.; Li, C., et al. Understanding the Low-Voltage Hysteresis of Anionic Redox in Na2Mn3O7. *Chemistry of Materials* **2019**, *31*, 3756–3765.

(24) Maitra, U.; House, R. A.; Somerville, J. W.; Tapia-Ruiz, N.; Lozano, J. G.; Guerrini, N.; Hao, R.; Luo, K.; Jin, L.; Pérez-Osorio, M. A., et al. Oxygen redox chemistry without excess alkali-metal ions in Na 2/3 [Mg 0.28 Mn 0.72] O 2. *Nature chemistry* **2018**, *10*, 288.

(25) Wu, J.; Zhuo, Z.; Rong, X.; Dai, K.; Lebens-Higgins, Z.; Sallis, S.; Pan, F.; Piper, L. F.; Liu, G.; Hussain, Z., et al. Dissociate lattice oxygen redox reactions from capacity and voltage drops of battery electrodes. *Science advances* **2020**, *6*.

(26) Kresse, G.; Furthmüller, J. Efficiency of ab-initio total energy calculations for metals and semiconductors using a plane-wave basis set. *Computational Materials Science* **1996**, *6*, 15 – 50.

(27) Kresse, G.; Joubert, D. From ultrasoft pseudopotentials to the projector augmented-wave method. *Phys. Rev. B* **1999**, *59*, 1758–1775.

(28) Sun, J.; Ruzsinszky, A.; Perdew, J. P. Strongly Constrained and Appropriately Normed Semilocal Density Functional. *Phys. Rev. Lett.* **2015**, *115*, 036402.

(29) Yang, J. H.; Kitchaev, D. A.; Ceder, G. Rationalizing accurate structure prediction in the meta-GGA SCAN functional. *Phys. Rev. B* **2019**, *100*, 035132.

(30) Zhang, Y.; Kitchaev, D. A.; Yang, J.; Chen, T.; Dacek, S. T.; Sarmiento-Pérez, R. A.; Marques, M. A.; Peng, H.; Ceder, G.; Perdew, J. P.; Sun, J. Efficient first-principles prediction of solid stability: Towards chemical accuracy. *npj Computational Materials* **2018**, *4*, 1–6.

(31) Langreth, D.; Perdew, J. The exchange-correlation energy of a metallic surface. *Solid State Communications* **1975**, *17*, 1425 – 1429.

(32) Harl, J.; Kresse, G. Accurate Bulk Properties from Approximate Many-Body Techniques. *Phys. Rev. Lett.* **2009**, *103*, 056401.

(33) Shishkin, M.; Kresse, G. Self-consistent *GW* calculations for semiconductors and insulators. *Phys. Rev. B* **2007**, *75*, 235102.

(34) Ong, S. P.; Richards, W. D.; Jain, A.; Hautier, G.; Kocher, M.; Cholia, S.; Gunter, D.; Chevrier, V. L.; Persson, K. A.; Ceder, G. Python Materials Genomics (pymatgen): A robust, open-source python library for materials analysis. *Comp. Mater. Sci.* **2013**, *68*, 314 – 319.

(35) Campbell, B. J.; Stokes, H. T.; Tanner, D. E.; Hatch, D. M. *ISODISPLACE*: a web-based tool for exploring structural distortions. *Journal of Applied Crystallography* **2006**, *39*, 607–614.

(36) Adamczyk, E.; Pralong, V. Na2Mn3O7: a suitable electrode material for Na-ion batteries? *Chemistry of Materials* **2017**, *29*, 4645–4648.

(37) Reed, J.; Ceder, G. Role of electronic structure in the susceptibility of metastable transition-metal oxide structures to transformation. *Chemical reviews* **2004**, *104*, 4513–4534.

(38) Guerrini, N.; Jin, L.; Lozano, J. G.; Luo, K.; Sobkowiak, A.; Tsuruta, K.; Massel, F.; Duda, L.-C.; Roberts, M. R.; Bruce, P. G. Charging Mechanism of Li2MnO3. *Chemistry of Materials* **2020**, *32*, 3733–3740.

(39) Taylor, Z. N.; Perez, A. J.; Coca-Clemente, J. A.; Braga, F.; Drewett, N. E.; Pitcher, M. J.; Thomas, W. J.; Dyer, M. S.; Collins, C.; Zanella, M., et al. Stabilization of O-O Bonds by d0 Cations in Li4+xNi1-xWO6 (0 ¡ x ¡ 0.25) Rock Salt Oxides as the

Origin of Large Voltage Hysteresis. *Journal of the American Chemical Society* **2019**, *141*, 7333–7346.

(40) Ren, X.; Rinke, P.; Joas, C.; Scheffler, M. Random-phase approximation and its applications in computational chemistry and materials science. *Journal of Materials Science* **2012**, *47*, 7447–7471.

(41) Schueller, E. C.; Zuo, J. L.; Bocarsly, J. D.; Kitchaev, D. A.; Wilson, S. D.; Seshadri, R. Modeling the structural distortion and magnetic ground state of the polar lacunar spinel GaV_4Se_8. *Phys. Rev. B* **2019**, *100*, 045131.

(42) Aydinol, M. K.; Kohan, A. F.; Ceder, G.; Cho, K.; Joannopoulos, J. Ab initio study of lithium intercalation in metal oxides and metal dichalcogenides. *Phys. Rev. B* **1997**, *56*, 1354–1365.

(43) Van der Ven, A.; Aydinol, M. K.; Ceder, G.; Kresse, G.; Hafner, J. First-principles investigation of phase stability in Li_xCoO_2. *Phys. Rev. B* **1998**, *58*, 2975–2987.

(44) Wolverton, C.; Zunger, A. First-Principles Prediction of Vacancy Order-Disorder and Intercalation Battery Voltages in Li_xCoO_2. *Phys. Rev. Lett.* **1998**, *81*, 606–609.

(45) Maintz, S.; Deringer, V. L.; Tchougréeff, A. L.; Dronskowski, R. LOBSTER: A tool to extract chemical bonding from plane-wave based DFT. *Journal of Computational Chemistry* **2016**, *37*, 1030–1035.

(46) Sudayama, T.; Uehara, K.; Mukai, T.; Asakura, D.; Shi, X.-M.; Tsuchimoto, A.; Mortemard de Boisse, B.; Shimada, T.; Watanabe, E.; Harada, Y.; Nakayama, M.; Okubo, M.; Yamada, A. Multiorbital bond formation for stable oxygen-redox reaction in battery electrodes. *Energy Environ. Sci.* **2020**,

(47) Hu, E.; Yu, X.; Lin, R.; Bi, X.; Lu, J.; Bak, S.; Nam, K.-W.; Xin, H. L.; Jaye, C.; Fischer, D. A., et al. Evolution of redox couples in Li-and Mn-rich cathode materials

and mitigation of voltage fade by reducing oxygen release. *Nature Energy* **2018**, *3*, 690–698.

(48) Xie, Y.; Saubanère, M.; Doublet, M.-L. Requirements for reversible extra-capacity in Li-rich layered oxides for Li-ion batteries. *Energy Environ. Sci.* **2017**, *10*, 266–274.

(49) Saha, S.; Assat, G.; Sougrati, M. T.; Foix, D.; Li, H.; Vergnet, J.; Turi, S.; Ha, Y.; Yang, W.; Cabana, J., et al. Exploring the bottlenecks of anionic redox in Li-rich layered sulfides. *Nat. Energy* **2019**, *4*, 977–987.

(50) Flamary-Mespoulie, F.; Boulineau, A.; Martinez, H.; Suchomel, M. R.; Delmas, C.; Pecquenard, B.; Cras, F. L. Lithium-rich layered titanium sulfides: Cobalt- and Nickel-free high capacity cathode materials for lithium-ion batteries. *Energy Storage Materials* **2020**, *26*, 213 – 222.

(51) Shinova, E.; Zhecheva, E.; Stoyanova, R.; Bromiley, G. D. High-pressure synthesis of solid solutions between trigonal LiNiO2 and monoclinic Li[Li1/3Ni2/3]O2. *Journal of Solid State Chemistry* **2005**, *178*, 1661 – 1669.